AGU PUBLICATIONS

Geophysical Research Letters

RESEARCH LETTER
10.1002/2016GL069215

Special Section:
First results from NASA's Magnetospheric Multiscale (MMS) Mission

Electron energization and mixing observed by MMS in the vicinity of an electron diffusion region during magnetopause reconnection

Li-Jen Chen[1,2], Michael Hesse[1], Shan Wang[1,2], Daniel Gershman[1,2], Robert Ergun[3], Craig Pollock[1], Roy Torbert[4], Naoki Bessho[1,2], William Daughton[5], John Dorelli[1], Barbara Giles[1], Robert Strangeway[6], Christopher Russell[6], Yuri Khotyaintsev[7], Jim Burch[8], Thomas Moore[1], Benoit Lavraud[9,10], Tai Phan[11], and Levon Avanov[1,2]

[1]NASA Goddard Space Flight Center, Greenbelt, MD, USA, [2]Astronomy Department, University of Maryland, College Park, MD, USA, [3]Department of Astrophysical and Planetary Sciences, University of Colorado Boulder, Boulder, Colorado, USA, [4]Department of Physics, University of New Hampshire, Durham, New Hampshire, USA, [5]Los Alamos National Laboratory, Los Alamos, New Mexico, USA, [6]Department of Earth, Planetary, and Space Sciences, University of California, Los Angeles, California, USA, [7]Swedish Institute of Space Physics, Uppsala, Sweden, [8]Southwest Research Institute, San Antonio, Texas, USA, [9]Institut de Recherche en Astrophysique et Plantologie, Universit de Toulouse, France, [10]Centre National de la Recherche Scientifique, Toulouse, France, [11]Space Science Laboratory, University of California, Berkeley, California, USA

Key Points:
- Distribution functions of accelerated meandering electrons in the diffusion region are observed
- Effects of meandering electrons on the electric field normal to the reconnection layer are detected
- Mixing of the inflowing and exhaust electrons shapes the exhaust flow pattern

Correspondence to:
L.-J. Chen,
li-jen.chen@nasa.gov

Citation:
Chen, L.-J., et al. (2016), Electron energization and mixing observed by MMS in the vicinity of an electron diffusion region during magnetopause reconnection, *Geophys. Res. Lett.*, *43*, 6036–6043, doi:10.1002/2016GL069215.

Received 15 APR 2016
Accepted 3 JUN 2016
Accepted article online 8 JUN 2016
Published online 28 JUN 2016

Abstract Measurements from the Magnetospheric Multiscale (MMS) mission are reported to show distinct features of electron energization and mixing in the diffusion region of the terrestrial magnetopause reconnection. At the ion jet and magnetic field reversals, distribution functions exhibiting signatures of accelerated meandering electrons are observed at an electron out-of-plane flow peak. The meandering signatures manifested as triangular and crescent structures are established features of the electron diffusion region (EDR). Effects of meandering electrons on the electric field normal to the reconnection layer are detected. Parallel acceleration and mixing of the inflowing electrons with exhaust electrons shape the exhaust flow pattern. In the EDR vicinity, the measured distribution functions indicate that locally, the electron energization and mixing physics is captured by two-dimensional reconnection, yet to account for the simultaneous four-point measurements, translational invariant in the third dimension must be violated on the ion-skin-depth scale.

1. Introduction

Magnetic reconnection is one of the most effective processes to energize plasmas and enhance mixing of otherwise disjoint magnetized plasma regimes [*Paschmann et al.*, 2013, and references therein]. Within the ion diffusion region, acceleration by parallel electric fields leading to pronounced temperature anisotropies has been observed in magnetotail reconnection [*Chen et al.*, 2008, 2009; *Egedal et al.*, 2010], and magnetopause reconnection [*Graham et al.*, 2014; *Lavraud et al.*, 2016], consistent with simulation predictions [*Chen et al.*, 2008; *Egedal et al.*, 2010]. Within the electron diffusion region (EDR), mixing of electrons with different energization histories is predicted by two-dimensional (2-D) particle-in-cell (PIC) simulations and theories to produce distribution functions with distinct features such as discrete striations, triangular structures, and crescent populations in asymmetric reconnection [*Hesse et al.*, 2014; *Bessho et al.*, 2016; *Chen et al.*, 2016] and symmetric reconnection [*Ng et al.*, 2011; *Bessho et al.*, 2014; *Shuster et al.*, 2015]. Electron acceleration by parallel electric fields leading to intense parallel currents has been reported in a magnetopause EDR event detected by Cluster [*Mozer et al.*, 2005; *Mozer and Pritchett*, 2011]. A demagnetized EDR is recorded by the Polar spacecraft [*Scudder et al.*, 2012]. Nonetheless, the EDR distribution function features are only simulation products until the 3-D electron measurements made by the Magnetospheric Multiscale (MMS) mission with a cadence 2 orders of magnitude higher than that in previous space missions.

Signatures of accelerated meandering magnetosheath (sheath) electrons have been observed by MMS in the magnetosphere (sphere) part of the EDR during magnetopause reconnection [*Burch et al.*, 2016]. Finite gyroradius effects of the meandering sheath electrons are resolved as a distinct crescent structure and seen to prevail in the vicinity of the stagnation point, as predicted by 2-D PIC simulations [*Hesse et al.*, 2014; *Bessho et al.*, 2016; *Chen et al.*, 2016; *Shay et al.*, 2016]. In the simulations, the sheath part of the EDR is characterized

by mixing of accelerated meandering electrons that spread out in the velocity dimension along the reconnection electric field and form a triangular distribution [*Chen et al.*, 2016] (hereafter referred as paper1). In the present paper, we report the first observation on the sheath EDR and the associated electron energization and mixing.

2. MMS Data

The observation data are from the Magnetospheric Multiscale (MMS) mission [*Burch et al.*, 2015, 2016] whose key science target is the kinetic physics of magnetic reconnection. The plasma data are from the Fast Plasma Investigation (FPI) suite, using the highest cadence mode in which the Dual Electron Spectrometer and Dual Ion Spectrometer detectors of FPI offer full three-dimensional (3-D) electron and ion velocity distribution functions (DFs) in the energy range 10 eV to 30 keV every 30 ms and 150 ms, respectively [*Pollock et al.*, 2016]. The magnetic field data are from the Fluxgate Magnetometer [*Russell et al.*, 2014] at 128 samples/second and electric field data at 8192 samples/second from the spin plane [*Lindqvist et al.*, 2014] and axial [*Ergun et al.*, 2014] double probes in the FIELDS suites [*Torbert et al.*, 2014].

The event examined below is from the dusk flank of the Earth's magnetopause. The MMS location in GSM is $[X, Y, Z] = [6.3, 5.4, -3]\ R_E$. Throughout this paper, an *LMN* coordinate will be employed with *N* determined by the minimum variance (positive toward the sheath), *L* the maximum variance of the magnetic field during a magnetopause crossing by MMS3 at 19 September 2015/074408–074454 UT, and *M* completes the third orthogonal axis (Figure 1b).

3. Results

An electron diffusion region is encountered by MMS during the reversals of ion jets and magnetic fields, as will be established in Figures 1–3. The spacecraft separation (Figure 1a) is about 1–2 d_i (1 $d_i \sim 42$ km based on the sheath upstream density 30 cm^{-3} taken from 0750 UT). A schematic showing the coordinate system and a simplified magnetic field configuration illustrates the signs of the magnetic field components B_L and B_N in regions surrounding the reconnection X line (Figure 1b). The component B_L (Figure 1c) from all four spacecraft shows that B_L at MMS4 (blue) is the least negative of the four and varies from −50 nT (sheath side of the current sheet) at 074326 UT to 50 nT (sphere side of the current sheet) at 074330.5 UT, while MMS3 (green) makes a very brief excursion to positive B_L, and MMS2 (red) and MMS1 (black) remain in the sheath side of the B_L reversal during the entire interval.

At the time marked as "EDR" MMS3 is on a steep climb from a sheath-B_L (negative) to a reversal, while MMS4 is at a sphere-B_L (∼45 nT) and MMS2&1 farther out in the $B_L < 0$ region. As a reference, the B_L in the sphere upstream is 60 nT (at 0740 UT) and the sheath upstream −55 nT (0750 UT). The *N* locations of the spacecraft indicate that MMS4 is the closest to the Earth, and MMS3 is closer than MMS2&1, consistent with the above B_L variations. The density (Figure 1d) varies from about 30 cm^{-3} to 20 cm^{-3} for MMS1-3 while decreases to 10 cm^{-3} for MMS4 at peak B_L. The V_{iL} reversal from −250 km/s (slightly larger amplitude than the upstream sheath Alfvén speed $V_A \sim 230$ km/s at 0750 UT) to ∼150 km/s is registered by all four spacecraft (Figure 1e). The electron flow component V_{eM} (Figure 1f) displays a steady sheath convection flow at approximately −150 km/s at ∼074325 UT and rises to ∼920 km/s (4 V_A) at MMS3 and ∼750 km/s at MMS4. The highly enhanced V_{eM} occurring in the vicinity of the B_L and V_{iL} reversals marks the visit of MMS3 to the sheath part of the EDR (note that the EDR indicated by the vertical line is a region to be further confirmed in Figures 2 and 3). MMS4 likely encounters the EDR farther downstream from the X line than MMS3, as it observes similarly steep B_L rise and V_{eM} enhancement (Figure 1), but at a larger B_N (not shown) than that registered by MMS3. To consolidate whether the MMS4 peak V_{eM} is also part of the EDR will be left for future work.

A close view of the EDR encounter by MMS3 is presented in Figure 2. The 6 s interval is almost entirely within the ion diffusion region as signatures of unmagnetized ions accelerated by the reconnection electric field are observed by all four spacecraft from ∼074326.4–074332 UT. Examples of the ion distributions showing demagnetization and acceleration signatures from this period can be found in *Wang et al.* [2016]. The peak V_{eM} (Figure 2b) occurs at a sharp gradient of B_L when B_M and B_N are vanishingly small (Figure 2a) and is thus nearly identical to $V_{e\perp}$ (Figure 2c, red). Three consecutive data points comprising the $V_{e\perp}$ peak deviate from the $E \times B$ velocity (Figure 2c, black) and the perpendicular ion velocity (Figure 2c, blue). The yellow curves mark the error bars of $V_{E\times B}$. The errors in $V_{e\perp}$ and $V_{i\perp}$ are only a few km/s and not shown. Each of the three data

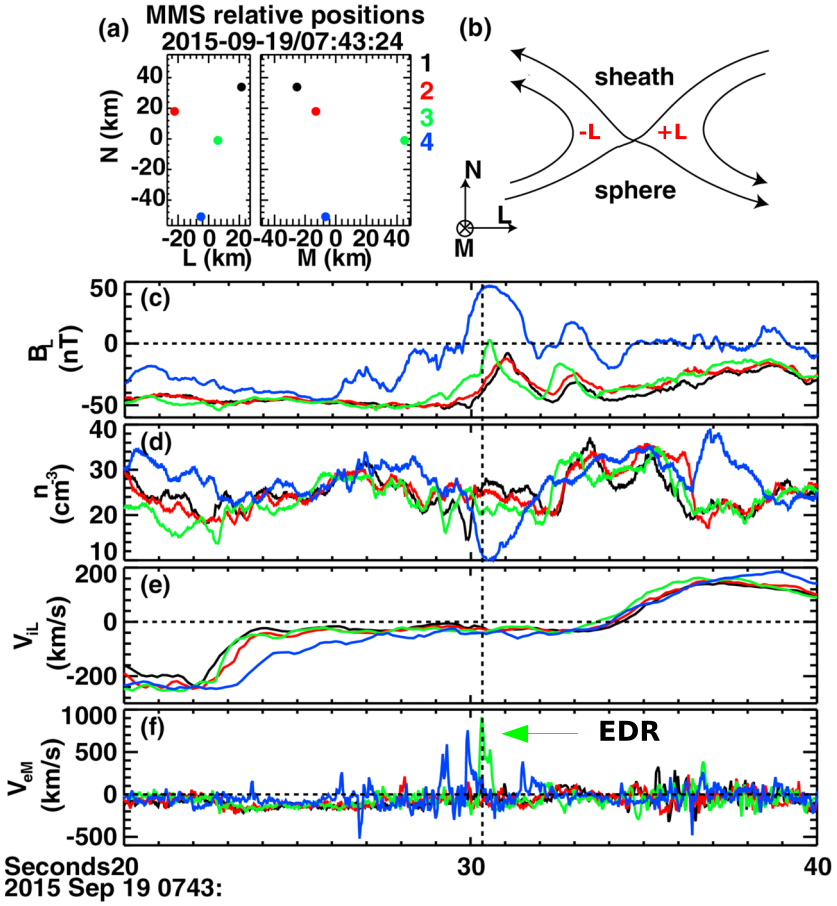

Figure 1. The MMS four-spacecraft perspective of the diffusion region encounter. (a) Spacecraft relative positions. (b) Schematic showing the coordinate system and a simplified magnetic field configuration of magnetopause reconnection. (c) At the time of the EDR encounter by MMS3, the magnetic field component B_L shows that MMS3 is on a steep climb from a sheath-B_L (~−13 nT) to a reversal, while MMS4 is at a sphere-B_L (~45 nT) and MMS2 and MMS1 farther out in the $B_L < 0$ region. (d) The density n is approximately 20 cm^{-3} at MMS3 , 10 cm^{-3} at MMS4, and 25 cm^{-3} at MMS2&1. (e) An ion jet reversal from approximately −250 km/s to 150 km/s is observed by all four spacecraft. (f) The electron out-of-plane flow V_{eM} rises to super-Alfvén speed (V_A ~230 km/s) at MMS3 and also at MMS4 right before 074330 UT when B_L has just turned positive. Note that the ambient sheath flow V_{eM} ~150 km/s is detected by all four spacecraft at around 074325 UT.

points at the V_{eM} peak comes from a 3-D DF that consists of 32 azimuthal and 16 polar angular and 32 energy bins—a total of 16,384 data points. We will examine representative EDR DFs in depth in Figure 3.

The peak V_{eM} at 920 km/s and the corresponding V_{iM} at −140 km/s (150 ms cadence) in a density 20 cm^{-3} give rise to a current density $J_M \sim -3.4$ μA/m^2. The steady perpendicular flow in V_e, V_i, and $V_{E\times B}$ at approximately 150 km/s at 074326–074327 UT is the ambient sheath convection.

The electric field normal to the reconnection layer, E_N, has a negative excursion in the sheath part of the EDR as shown by PIC simulations [*Chen et al.*, 2016] (Figure 3m) and laboratory experiments (J. Yoo, PPPL, private communication). The negative E_N is captured by MMS3 at the time of the peak V_{eM}. The E_N magnitude is significantly smaller than $|(V_e \times B)_N|$ (Figure 2d) for the same three data points whose $V_{e\perp}$ deviates from $V_{E\times B}$. The dominant contribution to the larger $|(V_e \times B)_N|$ than $|E_N|$ comes from $|V_{eM}B_L|$, and hence, the physics giving rise to the V_{eM} peak is responsible for the deviation between E_N and $(V_e \times B)_N$. We will return to this point in Figure 3.

The electron perpendicular temperature $T_{e\perp}$ (Figure 2e) reaches its peak values (~60 eV) and exceeds the parallel temperature $T_{e\|}$ in the region where E_N is negative, indicating enhanced perpendicular energization. On both sides of the $T_{e\perp}$ peak in a roughly symmetric manner, $T_{e\|}$ rises to its maximum at approximately 70 eV.

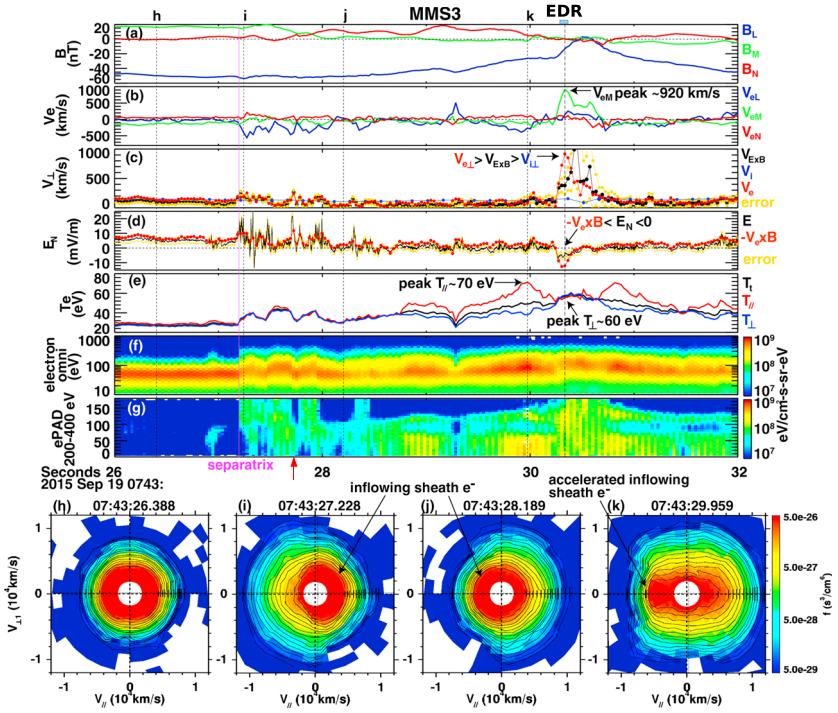

Figure 2. MMS3 measurements in the vicinity of the EDR (marked by a blue bar). (a) Magnetic field components showing that B_M and B_N are nearly zero at the V_{eM} peak. (b) Electron flow components. (c) Comparison of $V_{e\perp}$ with $V_{E\times B}$ and $V_{i\perp}$ showing $V_{e\perp} > V_{E\times B} > V_{i\perp}$ at the EDR. The yellow curves mark the uncertainty of $V_{E\times B}$. (d) The electric field component E_N has an amplitude smaller than that of $-V_e \times B$ at the EDR while highly fluctuating upon entering the separatrix (sharp boundary in Figures 2f and 2g just before the dotted vertical line i). (e) The electron temperatures parallel ($T_{e\|}$) and perpendicular ($T_{e\perp}$) to **B** and the total temperature (T_t). (f) The omnidirectional electron flux showing that the EDR electrons are significantly more energetic than the sheath electrons. (g) The pitch angle distribution of 200–400 eV electrons. (h–k) Electron DFs in the sheath within the ion diffusion region, in the separatrix region $+L$ of the X line, in the separatrix region $-L$ of X, in the exhaust at the peak $T_{e\|}$, respectively.

The energy of the peak omnidirectional flux also maximizes in the region of enhanced V_{eM} and negative E_N (Figure 2f).

To further see the electron energization and mixing recorded by MMS3 on its journey from the sheath into exhaust before arriving at the EDR, DF examples in $V_{\|}$-$V_{\perp 1}$ are displayed in Figures 2h–2k. The DFs are all gyrotropic, and hence, only the $V_{\|}$-$V_{\perp 1}$ slices are shown. The direction of $V_{\perp 1}$ is defined by $(b \times v) \times b$, where b and v are unit vectors of **B** and $\mathbf{V_e}$. The slices are obtained by averaging the phase-space density (PSD) in the velocity range 1000 km/s (~4 V_A) above and below the bulk $V_{\perp 2}$ (direction defined by $b \times v$). The sheath DF slice is nearly isotropic with $T_{e\|} \sim 28$ eV and $T_{e\perp} \sim 26$ eV (Figure 2h). Comparing to the upstream sheath $T_{e\|} \sim 24$ eV and $T_{e\perp} \sim 29$ eV at 0750 UT, the temperature change (increasing $T_{e\|}$ and decreasing $T_{e\perp}$) is consistent with conservation of magnetic moment causing $T_{e\perp}$ to decrease and parallel electric field acceleration leading to the $T_{e\|}$ increase [*Chen et al.*, 2009; *Lavraud et al.*, 2016].

In the sheath separatrix region, electron flows toward the X line have been predicted [*Pritchett*, 2008; *Chen et al.*, 2016], but the kinetic constitution for these flows has not been clarified. Here for the first time, MMS with its high-resolution DF measurements reveals the nature of these flows as mixing of the cold sheath and hot exhaust (EDR-accelerated and hot sphere) electrons. One such example is the DF near the sheath separatrix showing the inflowing sheath electrons in the $V_{\|} > 0$ half plane, diminishing sheath electrons going away from the X region (away-from-X) at $V_{\|} < 0$, and the hot exhaust electrons at $V_{\|} < 0$ (Figure 2i). The resulting flow is seen in $V_{eL} \sim -500$ km/s ($\mathbf{B} \sim \vec{B}_L$) toward the X line, and gives rise to an antiparallel current density approximately 2 μA/m² carried entirely by electrons. Note that the sizable net flow is dominated by the inflowing sheath electrons, as the away-from-X sheath component is diminished so much that the addition of hot exhaust electrons does not turn the flow away from the X line. A supporting comparison from PIC shows the flow pattern (V_{eL}) in the vicinity of the diffusion region (Figure 3o), and the inset panel demonstrates a DF

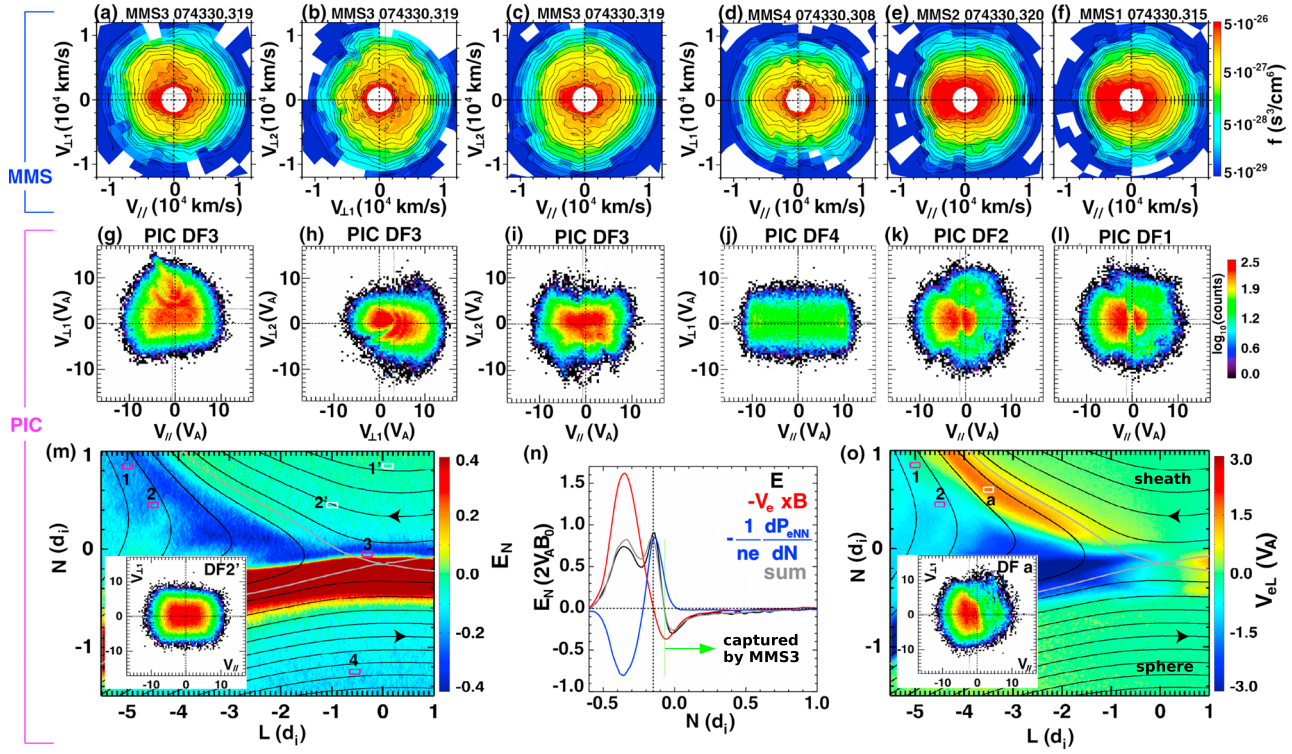

Figure 3. Comparisons of the DFs from the four MMS at the EDR time with 2-D PIC results. The MMS3 DF exhibits (a) a triangular shape in $V_{\parallel}$-$V_{\perp 1}$, (b) a crescent-like structure in $V_{\perp 1}$-$V_{\perp 2}$, and (c) parallel elongation at lower velocities while perpendicular elongation at higher velocities in $V_{\parallel}$-$V_{\perp 2}$. (d) MMS4 observes $T_{e\parallel} > T_{e\perp}$ at $B_L \sim 45$ nT. (e and f) MMS2&1 detect cold sheath remnants wrapped by hot electrons up to 135° pitch angles in the exhaust at the $-L$ side of the X line. (g–i) The PIC DF3 from a negative E_N layer (m) shows similar structures as those revealed in Figures 3a–3c, except that MMS3 observes more intense perpendicular energization than what the PIC simulation predicts. (j) PIC DF4 from the corresponding MMS4 location displays $T_{e\parallel} > T_{e\perp}$ in the sphere inflow region. (k and l) PIC DFs2&1 are taken from the exhaust at $-L$ side of the X line, and they each contain a sheath remnant population traveling opposite to **B**. (m) Structure of E_N with MMS locations (pink boxes mark where DFs 1–4 are taken) overplotted, and the inset shows DF2′ with electrons accelerated along **B** in the sheath inflow region. (n) The dominant terms contributing to E_N along N across the X line showing that $-V_e \times B$ and $-dP_{eNN}/dN/ne$ (the electric field due to meandering oscillations in N) sum up to the asymmetric bipolar E_N. The negative E_N excursion is captured by MMS3. (o) Structure of V_{eL} from PIC showing flows toward the X line along the sheath separatrices, and the white bin marks the location of PIC DFs shown in the inset demonstrating that diminishing sheath electrons away from the X line are the leading cause for the flows toward the X line.

example (DFa from location "a" marked in the V_{eL} panel) of a flow toward and in the $-L$ side (opposite to that of Figure 2i to keep Figure 3o compact) of the X line due to diminishing of the away-from-X sheath component.

Another example of mixing near the sheath separatrix is the DF just past 074328 UT (Figure 2j), and there at $V_{\parallel} < 0$ is the inflowing sheath population and at $V_{\parallel} > 0$ are the slightly diminished sheath population and the hot exhaust population. The resulting flow is nearly zero, a combined result from a small imbalance of sheath electrons along **B** and the hot exhaust electrons countering the inflowing sheath population. The above two separatrix DF examples demonstrate that the outstanding inflowing sheath population together with the sign of B_L enables the inference of whether the spacecraft is in the $+L$ or $-L$ side of the X line. The example in Figure 2i is from $+L$ (inflowing sheath at $V_{\parallel} > 0$ and $B_L < 0$—refer to Figure 1b to aid visualization) and that in Figure 2j $-L$ of the X line.

At the peak of $T_{e\parallel}$, the sheath-like population has been accelerated toward $-V_{\parallel}$ while maintaining similarly steep PSD gradient along $-V_{\parallel}$, and the hot component wraps around the sheath-like population to about 135° in pitch angle (Figure 2k). The acceleration is likely due to the parallel potential (integrated parallel electric fields along the magnetic field line) estimated to be ~90 eV based on the shoulder energy difference [*Egedal et al.*, 2010] in the parallel 1-D cuts (not shown) of DFs in Figures 2h and 2k. Here the flow is away from the X line ($V_{eL} < 0$), indicating that the inflowing sheath electrons fail to dominate the flow. The wrapping by the hot component is seen in the pitch angle distribution (PAD in Figure 2g) for 200–400 eV (0.85–1.2E4 km/s) electrons as the increase of the upper pitch angle range from approximately 90° at 074328 UT to 180° at the EDR, interpreted as due to reflection of hot exhaust electrons starting near PA 90° and covering an increasing

PA range as the spacecraft moves closer to the B_L reversal. The 200–400 eV electrons are regarded as hot exhaust electrons because they are more energetic than the sheath population (which drops to negligible values at about 200 eV—see Figure 2f at 074326–074327 UT) and only live in the exhaust side of the separatrix. The separatrix (vertical magenta line) is marked by the abrupt transition in the electron fluxes (Figures 2f and 2g), onset of enhanced E_N fluctuations, and sudden increases in $|V_{eL}|$ and T_e. The continuous presence of hot exhaust electrons when MMS3 transitions from the separatrix region $+L$ (Figure 2i) to that $-L$ (Figure 2j, for example, the first encounter with a DF similar to that in Figure 2j occurs at the time marked with a red arrow below Figure 2g) of the X line and the agreement between $V_{e\perp}$ and $V_{E\times B}$ (Figure 2c) during this interval imply that the spacecraft stays in the exhaust side of the separatrix and does not go through the EDR. Such a transition requires 3-D variations of the reconnection structure. The detailed scenario will be left for future investigations. Note that the $+L$ to $-L$ transition occurs when the ion flow V_{iL} remains roughly constant (~ -40) km/s amidst the jet reversal (Figure 1e), indicating that the ion jet reversal takes place on a much larger scale than does the $+L$ to $-L$ transition revealed by the electron DFs (Figures 2i and 2j).

We now examine the DF from the peak V_{eM} to further establish the EDR encounter by MMS3. The DFs measured right before and after the peak V_{eM} exhibit similar features, and hence, only the DF at the peak V_{eM} is presented (Figures 3a–3c). The slice of the DF in the $V_{\parallel}$-$V_{\perp 1}$ plane displays enhanced PSD forming a triangular shape in the $V_{\perp 1} > 0$ half plane (Figure 3a). The simultaneous magnetic field is dominated by B_L (~ -13 nT) and the electron velocity moment dominated by V_{eM}, and hence, $\hat{V}_{\parallel}$ is close to $-\hat{V}_L$ and $\hat{V}_{\perp 1}$ approximately $\hat{V}_M$. The triangular DF in $V_{\parallel}$-$V_{\perp 1}$ thus approximately translates to a triangular DF in V_L-V_M (not shown) which has been predicted to be an outstanding feature of the EDR distributions on the sheath side based on PIC simulations (paper1).

To provide close comparisons with the MMS data, DF slices in $V_{\parallel}$-$V_{\perp 1}$ from a PIC run are plotted (Figures 3g–3l) for locations marked by pink boxes and labeled as 1–4 in the E_N panel (Figure 3m). The V range for the DF slicing is $4V_A$, as is the case for the MMS DF slices. The PIC run uses the same parameters as in paper1 except for doubling of the average number of particles per cell to 6000. Location 3 corresponds to the MMS3 location constrained by (1) $B_L < 0$, $B_M \sim 0 \sim B_N$, (2) $-V_e \times B < E_N < 0$, (3) $V_{eM} \sim 4V_A$, and (4) the DFs corresponding to the three data points comprising the MMS3 V_{eM} peak. The allowed region for location 3 is within 0.5 d_i in L from the X line (little flexibility in N).

The most enhanced PSD in PIC DF3 (from location 3) exhibits a distinct triangle structure (Figure 3g). The triangle is due to mixing of sheath electrons that have bounced in the EDR for different numbers of times, as elucidated in paper1 for the reduced DFs in V_L-V_M. The specific triangular shape results from two acceleration processes: (1) the acceleration by the reconnection electric field E_M and (2) conversion of the L (parallel) momentum to M (perpendicular) by B_N, as understood for symmetric reconnection [*Bessho et al.*, 2014]. E_M at the MMS3 EDR time is inferred to be pointing in the $-M$ direction based on the corroborating observation facts that unmagnetized electrons are accelerated toward M (Figure 3a) and unmagnetized ions are accelerated toward $-M$ [*Wang et al.*, 2016]. The MMS E_M data are not shown, as the E field measurement errors due to the presence of cold plasmas and operation of the Active Spacecraft Potential Control prevent a conclusive detection. For the same reasons, $(E + V_e \times B)_{L,M}$ and $J \cdot (E + V_e \times B)$ are not presented.

The DF slice in $V_{\perp 1}$-$V_{\perp 2}$ (approximately V_M-V_N) presents a nongyrotropic crescent-like structure (Figure 3b), as a result of the unmagnetized sheath electrons carrying out their crescent orbits in $V_{\perp 1}$-$V_{\perp 2}$ (V_M-V_N) during meandering [*Chen et al.*, 2016; *Bessho et al.*, 2016]. The capability of MMS FPI to resolve scales below the electron gyroscale is critical to reveal the finite gyroradius signature of the accelerated meandering electrons. The crescent electron population having high PSD and dwelling in the $V_{\perp 1} > 0$ ($V_M > 0$) half plane is the main contributor to the large $V_{\perp}$ (V_{eM}) shown in Figure 2, consistent with the understanding obtained in paper1 for the EDR DFs from 2-D PIC asymmetric reconnection.

Note that crescent-like distributions can occur at any particle boundaries where the plasmas across the boundary differ significantly on their perpendicular temperatures (such as the separatrices during reconnection) and the distributions are sampled at scales well below the gyroscale of the high $T_{e\perp}$ plasma. In the case of Figure 3b, the crescent-like structure is due to the finite gyroradius effect of accelerated meandering electrons, captured in an ion jet reversal region where $|B_L|$ is on its steep descend to zero and $B_M \sim 0 \sim B_N$. Such magnetic field is specific to the X line vicinity, distinguishing the case from separatrices farther away from the X line where B_M and B_N are not vanishing.

The gyroradius of the electrons near the triangle tip in Figure 3a is larger than the magnetic field gradient scale. Electrons at the red tip of the triangular DF have $V_{\perp 1} \sim 6000$ km/s (comparing to 3245 km/s, the thermal speed of 60 eV electrons), corresponding to the maximum $V_{\perp 1}$ (V_M) of the crescent electrons in $V_{\perp 1}$-$V_{\perp 2}$ (V_M-V_N) and nearly zero $V_{\perp 2}$ (V_N), implying that the electrons are at the turning points of their bounces in N. Therefore, the gyroradius of these electrons can be estimated based on the magnetic field at $B_L/2$ using the B_L at the peak V_{eM} (see *Wang et al.* [2014] for a simple illustration) assuming that B_L depends linearly on N. The estimation yields 5.3 km, larger than the length scale of the magnetic gradient 3 km using MMS3 $|B|/|J|$ [*Hesse et al.*, 2016].

The $V_{\parallel}$-$V_{\perp 2}$ (close to V_L-V_N) DF in Figure 3c shows enhanced PSD in the positive and negative $V_{\perp 2}$, and the electrons with lower parallel velocities ($V_{\parallel} < 5000$ km/s) exhibit a field-aligned elongation, consistent with the sheath remnants that have been accelerated in the parallel direction (paper1). Comparing with the PIC DF3 in $V_{\parallel}$-$V_{\perp 2}$ (Figure 3i) and $V_{\perp 1}$-$V_{\perp 2}$ (Figure 3h), the MMS DF exhibits significantly more $V_{\perp 2}$ energization than that predicted by PIC.

The electron DFs measured by the other three spacecraft at the time of the MMS3 peak V_{eM} are presented in Figures 3d–3f to show the electron energization and mixing occurring 1–2 d_i away from the MMS3 location. These DFs are gyrotropic, and therefore, only the $V_{\parallel}$-$V_{\perp 1}$ slices are shown. The DF at MMS4 exhibits $T_{\parallel} > T_{\perp}$ (Figure 3d), qualitatively consistent with the temperature anisotropy in the PIC DF4 (Figure 3j) taken from the corresponding MMS4 location in PIC (relative to MMS3). Such T_e anisotropy is typical of reconnection electron inflow region within the ion diffusion region [*Chen et al.*, 2008; *Egedal et al.*, 2010; *Graham et al.*, 2014; *Lavraud et al.*, 2016].

The DFs detected by MMS2&1 have the sheath remnant population in $V_{\parallel} < 0$ and wrapped by the hot electrons up to PA 135°. The DFs in Figures 3e–3f and 2k share similar characteristics (and at similar B_L), implying that the locations of MMS2&1 are in the exhaust $-L$ of the X line. However, direct mapping of the MMS2&1 locations onto the PIC domain based on their relative positions to MMS3 places the two spacecraft in the sheath inflow region (marked as 1′ and 2′). We rule out the scenario of moving the sheath separatrix ($-L$ of the X line) to include both 1′ and 2′ in the exhaust, because the electron meandering dynamics will be drastically altered and inconsistency with the MMS3 data will arise. Alternatively, a twist of the X line in M within 1 d_i (approximately separation in M between MMS3 and MMS1&2) will accommodate both MMS1&2 in the exhaust $-L$ of the X line while keeping MMS3 and MMS4 in their respective locations. We therefore infer that variations in the M direction on the d_i scale are required to account for the four-point observations.

One collective effect of the meandering electrons is to cause the electric field E_N to deviate from $-(V_e \times B)_N$, as discerned for the first time in reality by MMS. The MMS3 data indicate that the difference between E_N and $-(V_e \times B)_N$ is due primarily to the large V_{eM} resulting from the crescent population in V_M-V_N ($V_{\perp 1}$-$V_{\perp 2}$) distribution. In other words, the meandering electrons forming the crescent population shown in Figure 3b are responsible for the deviation of E_N from $-(V_e \times B)_N$. Their contributions are through $-\mathrm{d}P_{eNN}/\mathrm{d}N/ne$, where P_{eNN} is the NN component of the electron pressure tensor. The electron force balance for E_N along N across the X line (result does not change appreciably within $L \pm 0.5d_i$) shows that the difference between E_N and $-(V_e \times B)_N$ is $-\mathrm{d}P_{eNN}/\mathrm{d}N/ne$ (Figure 3n). Physically speaking, this difference is due to the electric field caused by the electrons performing meandering oscillations in N, essentially the same physics as the bipolar E_N directing away from the current sheet center plane embedded in and opposite to the Hall electric field E_N in symmetric reconnection [*Chen et al.*, 2011].

4. Summary and Conclusion

The sheath part of an EDR in magnetopause reconnection is encountered by MMS. During the encounter, the following key features are observed: (1) a triangular structure in the electron DFs as a result of mixing of electrons that bounce in the EDR for different durations and hence gain different amounts of momentum from the reconnection electric field, (2) a crescent structure in the DFs due to the meandering crescent orbits in the velocity plane perpendicular to the reconnecting magnetic field, and (3) a normal electric field pointing to the sphere and weaker than $|-V_e \times B|$ owing to the electric field due to meandering electrons. In the vicinity of the EDR within the ion diffusion region, parallel acceleration in the inflow region as well as exhaust is observed as parallel elongations of the DFs, and results in parallel temperature increase. Mixing of hot exhaust electrons and cold sheath electrons with varying degrees of away-from-the-X-line component gives rise to flows and currents toward and away from the X line. Most of the observed energization and mixing features are consistent with PIC simulations of current sheet (2-D) reconnection, aside from the effects of upstream

temperature asymmetry and the likely present cold plasma in the sphere upstream that are not included in the simulations. However, to explain the simultaneous four-spacecraft observations, ion-skin-depth-scale variations in the out-of-plane dimension are required.

Acknowledgments
The research was supported in part by NSF grants AGS-1202537, AGS-1543598, and AGS-1552142 and at NASA GSFC by the Theory and Modeling Program and the Fast Plasma Investigation of the Magnetospheric Multiscale mission. Contribution from W.D. was supported by NASA Heliophysics Theory Program. The simulation run was performed on Pleiades under the NASA HEC Program. The MMS data are available at the MMS Science Data Center and PIC data upon request to the authors.

References

Bessho, N., L.-J. Chen, J. R. Shuster, and S. Wang (2014), Electron distribution functions in the electron diffusion region of magnetic reconnection: Physics behind the fine structures, *Geophys. Res. Lett.*, *24*, 8688–8695, doi:10.1002/2014GL062034.

Bessho, N., L.-J. Chen, and M. Hesse (2016), Electron distribution functions in the diffusion region of asymmetric magnetic reconnection, *Geophys. Res. Lett.*, *43*, 1828–1836, doi:10.1002/2016GL067886.

Burch, J. L., et al. (2015), Magnetospheric multiscale overview and science objectives, *Space Sci. Rev.*, *199*, 5–21, doi:10.1007/s11214-015-0164-9.

Burch, J. L., et al. (2016), Electron-scale measurements of magnetic reconnection in space, *Science*, *352*(6290), aaf2939, doi:10.1126/science.aaf2939.

Chen, L.-J., et al. (2008), Evidence of an extended electron current sheet and its neighboring magnetic island during magnetotail reconnection, *J. Geophys. Res.*, *113*, A12213, doi:10.1029/2008JA013385.

Chen, L.-J., et al. (2009), Multi-spacecraft observations of the electron current sheet, neighboring magnetic islands, and electron acceleration during magnetotail reconnection, *Phys. Plasmas*, *16*, 56501, doi:10.1063/1.3112744.

Chen, L.-J., W. S. Daughton, B. Lefebvre, and R. B. Torbert (2011), The inversion layer of electric fields and electron phase-space-hole structure during two-dimensional collisionless magnetic reconnection, *Phys. Plasmas*, *18*(1), 12904, doi:10.1063/1.3529365.

Chen, L.-J., M. Hesse, S. Wang, N. Bessho, and W. Daughton (2016), Electron energization and structure of the diffusion region during asymmetric reconnection, *Geophys. Res. Lett.*, *43*, 2405–2412, doi:10.1002/2016GL068243.

Egedal, J., A. Lê, N. Katz, L.-J. Chen, B. Lefebvre, W. Daughton, and A. Fazakerley (2010), Cluster observations of bidirectional beams caused by electron trapping during antiparallel reconnection, *J. Geophys. Res.*, *115*, A03214, doi:10.1029/2009JA014650.

Ergun, R., et al. (2014), The axial double probe and fields signal processing for the MMS mission, *Space Sci. Rev.*, doi:10.1007/s11214-014-0115-x.

Graham, D. B., Y. V. Khotyaintsev, A. Vaivads, M. André, and A. N. Fazakerley (2014), Electron dynamics in the diffusion region of an asymmetric magnetic reconnection, *Phys. Rev. Lett.*, *112*, 215004.

Hesse, M., N. Aunai, D. Sibeck, and J. Birn (2014), On the electron diffusion region in planar, asymmetric, systems, *Geophys. Res. Lett.*, *41*, 8673–8680, doi:10.1002/2014GL061586.

Hesse, M., et al. (2016), On the electron diffusion region in asymmetric reconnection with a guide magnetic field, *Geophys. Res. Lett.*, *43*, 2359–2364, doi:10.1002/2016GL068373.

Lavraud, B., et al. (2016), Currents and associated electron scattering and bouncing near the diffusion region at Earth's magnetopause, *Geophys. Res. Lett.*, *43*, 3042–3050, doi:10.1002/2016GL068359.

Lindqvist, P.-A., et al. (2014), The spin-plane double probe electric field instrument for MMS, *Space Sci. Rev.*, *199*, 137–165, doi:10.1007/s11214-014-0116-9.

Mozer, F. S., and P. L. Pritchett (2011), Electron physics of asymmetric magnetic field reconnection, *Space Sci. Rev.*, *158*, 119–143.

Mozer, F. S., S. D. Bale, J. P. McFadden, and R. B. Torbert (2005), New features of electron diffusion regions observed at subsolar magnetic field reconnection sites, *Geophys. Res. Lett.*, *32*, L24101, doi:10.1029/2005GL024092.

Ng, J., J. Egedal, A. Le, W. Daughton, and L.-J. Chen (2011), Kinetic structure of the electron diffusion region in antiparallel magnetic reconnection, *Phys. Rev. Lett.*, *106*(6), 65002, doi:10.1103/PhysRevLett.106.065002.

Paschmann, G., M. Øieroset, and T. Phan (2013), In-situ observations of reconnection in space, *Space Sci. Rev.*, *178*, 385–417, doi:10.1007/s11214-012-9957-2.

Pollock, C., et al. (2016), Fast plasma investigation for magnetospheric multiscale, *Space Sci. Rev.*, *199*, 331–406, doi:10.1007/s11214-016-0245-4.

Pritchett, P. L. (2008), Collisionless magnetic reconnection in an asymmetric current sheet, *J. Geophys. Res.*, *113*, A06210, doi:10.1029/2007JA012930.

Russell, C., et al. (2014), The magnetospheric multiscale magnetometers, *Space Sci. Rev.*, *199*, 189–256, doi:10.1007/s11214-014-0057-3.

Scudder, J. D., et al. (2012), First resolved observations of the demagnetized electron-diffusion region of an astrophysical magnetic-reconnection site, *Phys. Rev. Lett.*, *108*, 225005.

Shay, M. A., et al. (2016), Kinetic signatures of the region surrounding the X line in asymmetric (magnetopause) reconnection, *Geophys. Res. Lett.*, *43*, 4145–4154, doi:10.1002/2016GL069034.

Shuster, J. R., L.-J. Chen, M. Hesse, M. R. Argall, W. Daughton, R. B. Torbert, and N. Bessho (2015), Spatiotemporal evolution of electron characteristics in the electron diffusion region of magnetic reconnection: Implications for acceleration and heating, *Geophys. Res. Lett.*, *42*, 2586–2593, doi:10.1002/2015GL063601.

Torbert, R., et al. (2014), The fields instrument suite on MMS: Scientific objectives, measurements, and data products, *Space Sci. Rev.*, *199*, 105–135, doi:10.1007/s11214-014-0109-8.

Wang, S., et al. (2014), Hot magnetospheric O^+ and cold ion behavior in magnetopause reconnection: Cluster observations, *J. Geophys. Res. Space Pysics*, *119*, 9601–9623, doi:10.1002/2014JA020402.

Wang, S., et al. (2016), Ion demagnetization in the magnetopause current layer observed by MMS, *Geophys. Res. Lett.*, *43*, doi:10.1002/2016GL069406.